

Signal-Transformation-Based Repetitive Control of Spiral Trajectory for Piezoelectric Nanopositioning Stages

Zhao Feng , Student Member, IEEE, Jie Ling , Member, IEEE, Min Ming, Wenyu Liang , Member, IEEE, Kok Kiong Tan, Member, IEEE, and Xiaohui Xiao , Member, IEEE

Abstract—In this article, a novel signal-transformation-based repetitive controller (STBRC) dedicated to the accurate and fast tracking of spiral trajectory with a time-variant amplitude is proposed and tested. To overcome the requirement of strictly periodic references of conventional repetitive controller, a mapping between spiral trajectory and constant amplitude sinusoid is developed to provide multiple lower gains at the fundamental frequency and its harmonics of the spiral trajectory to ensure zero steady-state errors. The stability of the control method and convergence of steady-state errors are analyzed with a lifted-system representation, respectively, for its time-variant property. Compared with internal model-based controllers for this trajectory, STBRC has the advantages of a simpler structure, fewer parameters, and better performance. The application to a piezoelectric nanopositioning stage verifies the effectiveness of the proposed control method on suppression of cross-coupling errors and improving the tracking performance of high-speed spiral trajectory in comparison with other controllers.

Index Terms—Piezoelectric nanopositioning stage, repetitive control, signal transformation approach, spiral scan.

Manuscript received March 25, 2019; revised August 20, 2019 and December 30, 2019; accepted March 14, 2020. Date of publication March 19, 2020; date of current version June 15, 2020. Recommended by Technical Editor Professor X. Chen. This work was supported in part by the Shenzhen Science and Technology Program under Grant JCYJ20170306171514468, in part by China Postdoctoral Science Foundation under Grant 2018M642905, in part by China Scholarship Council (CSC) under Grant 201806270142, and in part by National Natural Science Foundation of China under Grant 51375349. (*Corresponding authors: Jie Ling; Xiaohui Xiao.*)

Zhao Feng is with the School of Power and Mechanical Engineering, Wuhan University, Wuhan 430072, China, and also with the Department of Electrical and Computer Engineering, National University of Singapore, Singapore 117576, Singapore (e-mail: fengzhaozhao7@whu.edu.cn).

Jie Ling, Min Ming, and Xiaohui Xiao are with the School of Power and Mechanical Engineering, Wuhan University, Wuhan 430072, China (e-mail: jamesling@whu.edu.cn; mingmin_whu@whu.edu.cn; xhxiao@whu.edu.cn).

Wenyu Liang and Kok Kiong Tan are with the Department of Electrical and Computer Engineering, National University of Singapore, Singapore 117576, Singapore, and also with the Institute for Infocomm Research (I2R), A*STAR, Singapore 138632, Singapore (e-mail: liangwenyu@u.nus.edu; kktan@nus.edu.sg).

Color versions of one or more of the figures in this article are available online at <http://ieeexplore.ieee.org>.

Digital Object Identifier 10.1109/TMECH.2020.2981966

I. INTRODUCTION

THE piezoelectric nanopositioning stage is a crucial scanning device aimed at operating with nanometer or subnanometer precision. It has the advantages of high stiffness and fast response through employing piezoelectric actuators and flexure-hinge-guided mechanisms [1], especially in the application of scanning probe microscopes (SPMs) manipulating matter at the molecular and atomic levels [2]. In general, the raster-based trajectory has been widely employed to construct the scanning image in the SPMs. The raster scanning involves driving the fast axis with a triangular trajectory and the slow axis with a staircase or ramp signal synchronously [3]. Due to the indigenous lightly damped resonant dynamics, the frequency of the triangular wave is typically restricted within 1 to 10% of the first resonance of these stages, which limits the scanning speed of SPMs significantly [4], [5].

To improve of tracking bandwidth for triangular waves, the general closed-loop feedback control strategies, such as adaptive control [6], sliding-mode control [7], [8], linear quadratic Gaussian (LQG) control [9], as well as negative-imaginary damping controllers, such as integral resonant control (IRC) [10], [11], have been proposed to minimize the residual vibration errors. In spite of significant improvements, the difficulties in tracking high-speed raster scanning remain.

Alternatively, the scanning speed can be increased by implementing nonraster patterns such as Lissajous, cycloid, and spiral methods based on the harmonic waveform at the expense of complex imaging processing in SPMs [4], [12]. In comparison with Lissajous and cycloid scanning patterns, the spiral trajectory can provide a uniform and well-defined image resolution at each point of the scanning area without retracing any part of the targeted area to achieve a higher scanning rate [13]. In the view of controller's design, the primary object for a triangular trajectory is to improve the tracking bandwidth to achieve a fast scanning. Generally, the bandwidth for a triangular trajectory should be approximately ten times the scanning frequency when the first five harmonics are considered. In comparison, the required bandwidth of a spiral scan is approximately 30% lower than the conventional raster scanning [12]. It should be noted that the amplitude of the spiral trajectory increases with tracking time. Therefore, the fast and precision tracking of spiral trajectory with converged error poses new challenges to controller design.

in contrast to Lissajous and cycloid trajectories with constant amplitude sinusoids. In [13], a positive position feedback controller was designed to track spiral trajectory with a high closed-loop bandwidth. A multi-input multi-output model predictive control scheme with a damping compensator was proposed to improve tracking speed [14]. In [15], a phase-locked loop-based proportional-integral (PI) controller was implemented to maintain the exact 90° phase shift of the spiral trajectory with the increasing scanning speed. However, the tracking errors with these methods still increase with the varying amplitude so that the scanning performance is significantly deteriorated.

In particular, the internal model controller (IMC) is a practice approach to achieve asymptotic tracking of reference signals with zero steady-state errors [16]. In [17], an IMC has been developed to track a Lissajous trajectory with constant amplitude sinusoids. Moreover, the internal model of a sinusoidal signal was incorporated into LQG controller for spiral scanning [18]. However, the phase error between the input and output is still significant because the built internal model was for constant amplitude sinusoidal signals. To cope with the varying amplitude sinusoidal reference, the IMC synthesized for spiral trajectory was proposed in [19] and [20] to make the tracking error convergent. Note that the nonlinearities such as hysteresis can result in errors in the high-order harmonics of the references [13], [21]. As a consequence, more than three IMC terms that contain high-frequency internal models should be augmented to the final controller, which increases the complexity of parameter computation, and once the frequency of references changes, the controller should be resynthesized.

The conventional repetitive controller (CRC) is also designed based on the internal model principle [16]. The main benefit of this controller lies in that it can provide infinite gains at the fundamental frequency as well as its harmonics of the reference or disturbance [22], [23]. The CRC has been successfully implemented on the piezoelectric nanopositioning stages to track raster trajectory [21], [24], [25]. It is notable that although the tracking errors with CRC can converge to zero with the increasing number of periodic motion, the anticipated reference should be strictly periodic. The CRC is not suitable to track spiral trajectory in spite that it can obtain infinite internal models with a simpler structure and fewer parameters compared with the mentioned IMC. In [26]–[29], a signal transformation approach was proposed and analyzed to improve the steady-state tracking performance while limiting the projected measurement noise. The method transforms the piece-wise linear (affine) references like triangular waveform to ramp signal and designs double-integrator to minimize errors. Although a signal transformation control approach to tracking arbitrary references has been proposed in [30], the reference signal must be continuous and periodic and, thus, is not suitable for the spiral trajectory.

The main objective of this article is to achieve high-speed and precision motion for piezoelectric nanopositioning stages with spiral trajectory. Inspired by the signal transformation approach, a signal-transformation-based repetitive controller (STBRC) is proposed in this article. Compared with IMC in [19] and [20], the proposed method has fewer parameters to be tuned, and is much

easier to implement with spiral trajectories at different frequencies. Furthermore, STBRC also extends the application of CRC that requires strictly periodic signals. The main contribution of this article is three fold. First, the signal transformation approach that converts between the spiral signal and constant amplitude sinusoid, augmented into CRC, i.e., STBRC, is developed to provide infinite gain at the harmonics of the spiral reference. Second, the stability and convergence of steady-state errors of the control method are analyzed with a lifted-system representation for the time-variant property of the controller. Third, the comparative experiments on a piezoelectric nanopositioning stage are performed to elucidate the effectiveness of STBRC on tracking spiral trajectory.

The rest of this article is organized as follows. The background of the spiral trajectory and CRC is showed in Section II. The controller design of STBRC as well as the relevant stability analysis is presented in Section III. Section IV gives the detailed experimental setup. Experiments on a piezoelectric nanopositioning stage and comparisons of the results are elaborated in Section V. Section VI concludes this article.

II. PRELIMINARIES OF SPIRAL TRAJECTORY AND CRC

A. Spiral Trajectory

In this article, the spiral of Archimedes with a constant angular velocity is adopted, which is generated for x - and y -axis by [12]

$$r_x(t) = A(t)\cos(2\pi ft); r_y(t) = A(t)\sin(2\pi ft) \quad (1)$$

where f is the scanning frequency and $A(t)$ is the amplitude varying with time t , which can be expressed as

$$A(t) = pft \quad (2)$$

where p is the pitch, the distance between two consecutive intersections of the spiral curve, can be determined by

$$p = \frac{\text{spiral radius} \times 2}{\text{number of curves} - 1}. \quad (3)$$

From (1), the spiral signal is a sinusoid multiplied by a linearly time-varying signal, which may lead to tracking error increasing with time especially for traditional feedback control, such as built-in PI controller.

B. Conventional Repetitive Controller

The CRC is an effective control algorithm based on internal model principle [16] to provide high gains at the harmonics of the reference trajectory to tracking periodic signals precisely through employing a signal generator $\frac{1}{1-z^{-N}}$, where N is the number of points per period of the reference. Considering a discrete single-input-single-output linear time-invariant (LTI) system $P(z)$ with time-shift operator z , the block diagram of discrete-time CRC with a plug-in implementation is demonstrated in Fig. 1, where $r(k)$ is the reference, $y(k)$ is the output of the plant, $e(k)$ is the tracking error, $u(k)$ is the control force, and $C(z)$, $L(z)$, and $Q(z)$ are the baseline feedback controller (FBC), learning filter, and low-pass filter to improve stability of CRC, respectively. z^{-m} is the compensated time delay caused by the nonminimum-phase characteristic of the piezoelectric

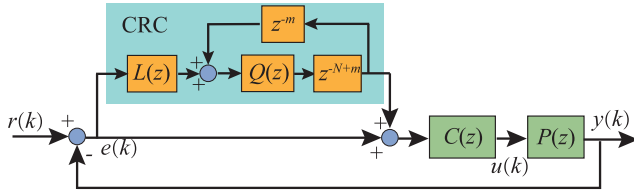


Fig. 1. Block diagram of CRC with a plug-in implementation. In this control scheme, $C(z)$ is a baseline FBC and CRC can be plugged into the control system without changing the exiting $C(z)$.

nano-positioning system. For a minimum-phase system, m can be set as zero. It can be seen in Fig. 1 that the CRC is plugged into the control system without changing the existed baseline FBC, which is easy to be implemented. From Fig. 1, the transfer function of CRC is given by

$$C_{\text{CRC}}(z) = \frac{L(z)Q(z)z^{-N+m}}{1 - Q(z)z^{-N}}. \quad (4)$$

The sensitivity transfer function $S_{\text{CRC}}(z)$ of CRC from $r(k)$ to $e(k)$ is obtained by

$$S_{\text{CRC}}(z) = \frac{1}{1 + [1 + C_{\text{CRC}}(z)]P(z)C(z)}. \quad (5)$$

By substituting (4) into (5) and rearranging terms, it can be deduced that

$$S_{\text{CRC}}(z) = \frac{[1 - Q(z)z^{-N}]S_{\text{fb}}(z)}{1 + Q(z)z^{-N}[z^m L(z)T_{\text{fb}}(z) - 1]} \quad (6)$$

where $S_{\text{fb}}(z)$ and $T_{\text{fb}}(z)$ are sensitivity transfer function and complementary sensitivity function with standalone FBC $C(z)$, i.e.,

$$S_{\text{fb}}(z) = \frac{1}{1 + P(z)C(z)}; T_{\text{fb}}(z) = \frac{P(z)C(z)}{1 + P(z)C(z)}. \quad (7)$$

According to Small Gain Theorem [31], the stability of CRC can be assured if

$$\begin{aligned} & \|Q(z)z^{-N}[z^m L(z)T_{\text{fb}}(z) - 1]\|_\infty \\ &= \|Q(z)[z^m L(z)T_{\text{fb}}(z) - 1]\|_\infty < 1. \end{aligned} \quad (8)$$

When $r(k)$ is a periodic signal with N samples in one period, $S_{\text{CRC}}(z) = 0$ because of $(1 - z^{-N})R(z)$ within the bandwidth of $Q(z)$, i.e., $|Q(z)|=1$, where $R(z)$ is the z -transformation of $r(k)$. Furthermore, the learning filter $L(z)$, cut-off frequency of $Q(z)$, and delay term m should be chosen properly to retain the stability of CRC. It should be noted that the analysis of the stability condition (8) is conducted in frequency domain that requires the closed-loop system to be LTI.

III. CONTROLLER DESIGN

A. Signal-Transformation-Based Repetitive Control

Inspired by the method in [26], [29], and [30], where the transformation between periodic piece-wise linear reference signals and a ramp reference signal were designed, a mapping between the spiral trajectory and constant amplitude sinusoid is proposed in this article. For a discrete-time system, with the

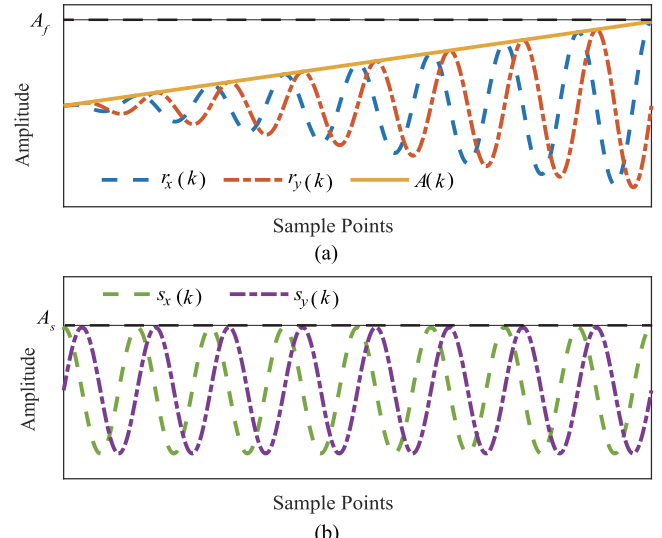


Fig. 2. Illustration of the signal transformation approach for spiral trajectory. (a) Desired references with the maximum amplitude A_f . (b) Transformed signals with the scaled constant amplitude A_s . The amplitude of spiral trajectory $r_x(k)$ and $r_y(k)$ increases with the envelope $A(k)$ and through the $\Phi_{\text{ST}}(k)$ the spiral trajectory is transformed to constant amplitude sinusoid $s_x(k)$ and $s_y(k)$.

signal transformation term $\Phi_{\text{ST}}(k)$ for x - and y -axis, it can be obtained that

$$s_x(k) = A_s \cos(2\pi f T_s k) = \Phi_{\text{ST}}(k) r_x(k) \quad (9)$$

$$s_y(k) = A_s \sin(2\pi f T_s k) = \Phi_{\text{ST}}(k) r_y(k) \quad (10)$$

where T_s is the sample time of the system, A_s is the scaled constant amplitude. Combining with (1) and (2), $\Phi_{\text{ST}}(k)$ can be presented in the follow form:

$$\Phi_{\text{ST}}(k) = \frac{A_s}{pf T_s k}. \quad (11)$$

Similarly, the transformation of constant amplitude sinusoid to spiral trajectory $\Phi_{\text{IST}}(k)$ is derived as

$$\Phi_{\text{IST}}(k) = \frac{pf T_s k}{A_s}. \quad (12)$$

An illustration of the signal transformation approach for a spiral trajectory is demonstrated in Fig. 2. On the one hand, the references of both x - and y -axis are converted to single-tone cosine and sinusoidal waves $s_x(k)$ and $s_y(k)$, respectively, which facilitates the controller design significantly. On the other hand, the original spiral trajectory can also be obtained via $\Phi_{\text{IST}}(k)$. This mapping between spiral trajectory and constant amplitude sinusoid is utilized to develop the proposed controller.

Considering one of motion directions of the piezoelectric nano-positioning stage, the proposed STBRC with a plug-in implementation is illustrated in Fig. 3. The actual input of the system is the scaled constant amplitude cosine or sinusoidal wave that is converted by $\Phi_{\text{ST}}(k)$. The block $\Phi_{\text{IST}}(k)$ between the controller and plant does the reverse action to generate spiral trajectory $y(k)$. As a consequence, $e(k)$ in Fig. 3 is the error caused by the periodic cosine or sinusoidal wave that can converge to zero via employing CRC.

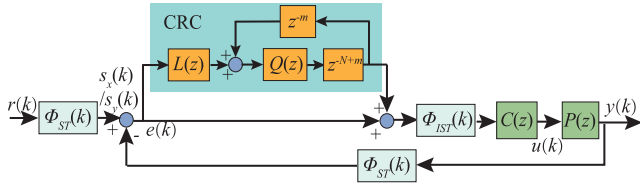


Fig. 3. Block diagram of STBRC with a plug-in implementation for spiral trajectory. Through the implementation of $\Phi_{ST}(k)$, the controller can be designed to track periodic signals and the usage of $\Phi_{IST}(k)$ makes the control force and output convert to the spiral trajectory.

To improve the convergence rate of STBRC, the design of the learning filter $L(z)$ is the inversion of the complementary sensitivity function $T_{fb}(z)$ in general. Note that the piezoelectric nanopositioning stage generally has nonminimum-phase zeros due to the noncollocated actuators and sensors [32]. Therefore, $T_{fb}(z)$ also contains nonminimum-phase zeros that limit the direct application of CRC strategy. In this article, the term z^{-m} is added to adjust the effects caused by the nonminimum-phase characteristic and $L(z)$ is calculated by the zero-magnitude-error tracking (ZMET) method [33]. For the nonminimum-phase plant $T_{fb}(z)$, the transfer function can be decomposed as

$$T_{fb}(z) = \frac{N_s(z)N_u(z)}{D(z)} \quad (13)$$

where N_s and N_u compose of stable and unstable zeros, respectively, and $D(z)$ contains all the stable and identified poles. Besides, N_u can be written as

$$N_u(z) = N_{u,n}z^n + N_{u,n-1}z^{n-1} + \dots + N_{u,0} \quad (14)$$

where n is the number of nonminimum-phase zeros. According to the ZMET method, the approximate inversion of $T_{fb}(z)$, i.e., $L(z)$ is given by

$$L(z) = \frac{D(z)z^{-d}}{N_s(z)N_u^*(z)} \quad (15)$$

where d is the delay steps to make the transfer function causal for practical implementation, and $N_u^*(z)$ is also a n -order polynomial by flipping the coefficients of $N_u(z)$, given by

$$N_u^*(z) = N_{u,0}z^n + N_{u,1}z^{n-1} + \dots + N_{u,n}. \quad (16)$$

It can be seen that for the nonminimum-phase plant, the learning filter always leads to delay in the error signal $e(k)$. Hence, an adjustable term m is added to STBRC design to achieve the anticipated performance.

It should be mentioned that it is not possible to establish a perfectly accurate model $P(z)$ in practice. To improve the robustness of the proposed controller to cope with model uncertainties in the high-frequency region, a zero-phase low-pass filter is employed as

$$Q(z) = az + b + az^{-1} \quad (17)$$

and a, b should satisfy $2a + b = 1$ to ensure a unit gain below the cut-off frequency [34]. Although $Q(z)$ improves the robustness, the tracking performance is deteriorated, especially for high-frequency errors. A tradeoff between stability and tracking

accuracy should be taken into consideration when selecting a and b .

Note that the nonlinear hysteresis effect is treated as external disturbances in this article. Generally, this nonlinearity generates errors with the infinite number of harmonics in addition to its fundamental component of the reference [17], [21]. Therefore, through the signal transformation, the hysteresis can also be mitigated through the proposed STBRC.

B. Stability and Performance Analysis

In this section, the stability and tracking performance are analyzed. For a clear expression, all the vectors are written as regular, lowercase, bold letters with the length N , and the matrices are regular, capital, bold letters with the dimension of $N \times N$.

Note that the time-variant terms $\Phi_{ST}(k)$ and $\Phi_{IST}(k)$ are included in the STBRC strategy so that the stability criterion (8) is not applicable to this article. Inspired by the time-domain analysis in iterative learning control [35], a lifted-system framework is adopted to deduce the stability of STBRC in this article. To construct the lifted-system representation, the plant $P(z)$ can also be expressed as a state-space model, i.e.,

$$\begin{aligned} \mathbf{x}_p(k+1) &= \mathbf{Ax}_p(k) + \mathbf{Bu}(k) \\ y(k) &= \mathbf{Cx}_p(k) + \mathbf{Du}(k) \end{aligned} \quad (18)$$

where $\mathbf{x}_p(k)$ is the state vector of $P(z)$ and $\mathbf{A}, \mathbf{B}, \mathbf{C}$, and \mathbf{D} are the state matrix, input matrix, output matrix, and feedthrough matrix, respectively. For a CRC system, the dynamics can also be deemed over the finite periods with N samples. Hence, the dynamics on the j th period of $P(z)$ are described in the equivalent lifted form as

$$\mathbf{y}(j) = \mathbf{Pu}(j) \quad (19)$$

where j is the current number of period and

$$\mathbf{P} = \begin{bmatrix} \mathbf{D} & 0 & \cdots & 0 \\ \mathbf{CD} & \mathbf{D} & \cdots & 0 \\ \vdots & \vdots & \ddots & \vdots \\ \mathbf{CA}^{N-2}\mathbf{D} & \mathbf{CA}^{N-3}\mathbf{D} & \cdots & \mathbf{D} \end{bmatrix} \quad (20)$$

$$\mathbf{u}(j) = [u(jN - N) \ u(jN + 1 - N) \ \dots \ u(jN - 1)]^\top \quad (21)$$

$$\mathbf{y}(j) = [y(jN - N) \ y(jN + 1 - N) \ \dots \ y(jN - 1)]^\top \quad (22)$$

where $\mathbf{u}(j)$ and $\mathbf{y}(j)$ are constructed by $u(k)$ and $y(k)$ with $k \in \{jN - N, jN + 1 - N, \dots, jN - 1\}$. When a delay is contained in the plant, a slight change of (20)–(22) should be made to enhance the similarity of the frequency-domain model [35].

To analyze the stability of STBRC, the block diagram of STBRC with a lifted-system representation at period j is presented in Fig. 4, where \mathbf{G}_d , \mathbf{L} , \mathbf{Q} are the lifted matrices of $P(z)C(z)$, $L(z)$, and $Q(z)$, respectively. \mathbf{M}^{-N+m} and \mathbf{M}^{-m} are the lifted representation of terms with $-N + m$ and m -step

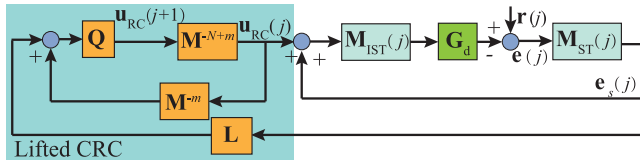


Fig. 4. Block diagram of STBRC with a lifted-system representation for stability and performance analysis. This block diagram is a time-domain presentation during the j th period.

delay. $\mathbf{M}_{\text{ST}}(j)$ and $\mathbf{M}_{\text{IST}}(j)$ are diagonal matrices, defined as

$$\mathbf{M}_{\text{ST}}(j) = \text{diag}[p_{\text{ST},1}(j) p_{\text{ST},k}(j), \dots, p_{\text{ST},N}(j)]^\top \quad (23)$$

$$\mathbf{M}_{\text{IST}}(j) = \text{diag}[p_{\text{IST},1}(j) p_{\text{IST},k}(j), \dots, p_{\text{IST},N}(j)]^\top \quad (24)$$

where the symbol $\text{diag}[\cdot]$ means the diagonal matrix with the vector \cdot as the main diagonal. Based on (11) and (12), it is found that

$$p_{\text{ST},k}(j) = \frac{A_s}{pf[T_s k + (j-1)T_p]} \quad (25)$$

$$p_{\text{IST},k}(j) = \frac{pf[T_s k + (j-1)T_p]}{A_s} \quad (26)$$

with $T_p = 1/f$.

To check the closed-loop stability of STBRC, the control force in the next period $\mathbf{u}_{\text{RC}}(j+1)$ is calculated according to that of current period $\mathbf{u}_{\text{RC}}(j)$ as

$$\begin{aligned} \mathbf{u}_{\text{RC}}(j+1) &= \mathbf{Q}[\mathbf{L}\mathbf{e}_s(j) + \mathbf{M}^{-m}\mathbf{u}_{\text{RC}}(j)] \\ &= \mathbf{Q}[\mathbf{L}\mathbf{M}_{\text{ST}}(j)\mathbf{e}(j) + \mathbf{M}^{-m}\mathbf{u}_{\text{RC}}(j)] \end{aligned} \quad (27)$$

and

$$\begin{aligned} \mathbf{e}(j) &= \mathbf{r}(j) - \mathbf{G}_d\mathbf{M}_{\text{IST}}(j)[\mathbf{u}_{\text{RC}}(j) + \mathbf{M}_{\text{ST}}(j)\mathbf{e}(j)] \\ &= \mathbf{r}(j) - \mathbf{G}_d\mathbf{M}_{\text{IST}}(j)\mathbf{u}_{\text{RC}}(j) - \mathbf{G}_d\mathbf{M}_{\text{IST}}(j)\mathbf{M}_{\text{ST}}(j)\mathbf{e}(j). \end{aligned} \quad (28)$$

Because $\mathbf{M}_{\text{ST}}(j)\mathbf{M}_{\text{IST}}(j) = \mathbf{I}$ generates a identity matrix, (28) can be rearranged as

$$\begin{aligned} \mathbf{e}(j) &= (1 + \mathbf{G}_d)^{-1}\mathbf{r}(j) - (1 + \mathbf{G}_d)^{-1}\mathbf{G}_d\mathbf{M}_{\text{IST}}(j)\mathbf{u}_{\text{RC}}(j) \\ &= \mathbf{S}_{\text{fb}}\mathbf{r}(j) - \mathbf{T}_{\text{fb}}\mathbf{M}_{\text{IST}}(j)\mathbf{u}_{\text{RC}}(j) \end{aligned} \quad (29)$$

where \mathbf{S}_{fb} and \mathbf{T}_{fb} are the lifted representation of (7). Substituting (29) into (27), it can be obtained that

$$\begin{aligned} \mathbf{u}_{\text{RC}}(j+1) &= \mathbf{Q}[\mathbf{M}^{-m} - \mathbf{L}\mathbf{M}_{\text{ST}}(j)\mathbf{T}_{\text{fb}}\mathbf{M}_{\text{IST}}(j)] \\ &\quad \times \mathbf{u}_{\text{RC}}(j) + \mathbf{Q}\mathbf{L}\mathbf{S}_{\text{fb}}\mathbf{M}_{\text{ST},j}\mathbf{r}(j). \end{aligned} \quad (30)$$

It is clear that for spiral trajectory, $\mathbf{M}_{\text{ST}}(j)\mathbf{r}(j)$ is the same sinusoid for each period and the lifted description of a pure delay term is an identity matrix. Hence, the controller is stable if

$$\rho(\mathbf{E}) = \rho[\mathbf{Q}(\mathbf{I} - \mathbf{L}\mathbf{M}_{\text{ST}}(j)\mathbf{T}_{\text{fb}}\mathbf{M}_{\text{IST}}(j))] < 1 \quad (31)$$

where $\rho(\cdot)$ is the maximum eigenvalue of the matrix. It should be noted that \mathbf{L} and \mathbf{T}_{fb} are both with lower triangular Toeplitz

structures defined in [35], which indicates that the eigenvalues of these matrices are the diagonal elements. Combining $\mathbf{M}_{\text{ST}}(j)\mathbf{M}_{\text{IST}}(j) = \mathbf{I}$ and the property of diagonal matrix, $\mathbf{I} - \mathbf{L}\mathbf{M}_{\text{ST}}(j)\mathbf{T}_{\text{fb}}\mathbf{M}_{\text{IST}}(j)$ remains a lower triangular matrix so that $\rho[\mathbf{L}\mathbf{M}_{\text{ST}}(j)\mathbf{T}_{\text{fb}}\mathbf{M}_{\text{IST}}(j)] = \rho(\mathbf{L}\mathbf{T}_{\text{fb}})$. When $Q(z)$ is a causal low-pass filter, it can be concluded that

$$\rho[\mathbf{Q}(\mathbf{I} - \mathbf{L}\mathbf{M}_{\text{ST}}(j)\mathbf{T}_{\text{fb}}\mathbf{M}_{\text{IST}}(j))] = \rho[\mathbf{Q}(\mathbf{I} - \mathbf{L}\mathbf{T}_{\text{fb}})]. \quad (32)$$

As shown in (32), it is evident that the scaled constant amplitude A_s and the transformation terms $\Phi_{\text{ST}}(k)$, $\Phi_{\text{IST}}(k)$ have no influence on the stability of STBRC.

In order to investigate the steady-state error of the proposed controller, the steady-state command signal $\mathbf{u}_{\text{RC},ss}$ can be derived from (30) as

$$\mathbf{u}_{\text{RC},ss} = \frac{\mathbf{Q}\mathbf{L}\mathbf{S}_{\text{fb}}\mathbf{M}_{\text{ST}}(j)\mathbf{r}(j)}{\mathbf{I} - \mathbf{Q}[\mathbf{M}^{-m} - \mathbf{L}\mathbf{M}_{\text{ST}}(j)\mathbf{T}_{\text{fb}}\mathbf{M}_{\text{IST}}(j)]}. \quad (33)$$

Therefore, the steady-state output \mathbf{y}_{ss} is given by

$$\mathbf{y}_{ss} = \mathbf{G}_d\mathbf{M}_{\text{IST}}(j)[\mathbf{u}_{\text{RC},ss} + \mathbf{M}_{\text{ST}}(j)\mathbf{e}_{ss}] \quad (34)$$

and the steady-state error \mathbf{e}_{ss} can be calculated as

$$\mathbf{e}_{ss} = \mathbf{r}(j) - \mathbf{y}_{ss} = \mathbf{r}(j) - \mathbf{G}_d\mathbf{M}_{\text{IST}}(j)[\mathbf{u}_{\text{RC},ss} + \mathbf{M}_{\text{ST}}(j)\mathbf{e}_{ss}]. \quad (35)$$

After simplification, the abovementioned equation can be rewritten as

$$\mathbf{e}_{ss} = \mathbf{S}_{\text{fb}}\mathbf{r}(j) - \mathbf{T}_{\text{fb}}\mathbf{M}_{\text{IST}}(j)\mathbf{u}_{\text{RC},ss}. \quad (36)$$

Taking (33) into (36), it can be deduced as

$$\mathbf{e}_{ss} = \frac{\mathbf{I} - \mathbf{Q}\mathbf{M}^{-m}}{\mathbf{I} - \mathbf{Q}[\mathbf{M}^{-m} - \mathbf{L}\mathbf{M}_{\text{ST}}(j)\mathbf{T}_{\text{fb}}\mathbf{M}_{\text{IST}}(j)]}\mathbf{S}_{\text{fb}}\mathbf{r}(j). \quad (37)$$

From (37), it can be obtained that for the error within the bandwidth of the low-pass filter $Q(z)$, $|Q(z)| = 1$, the amplitude of the numerator is $|\mathbf{I} - \mathbf{Q}\mathbf{M}^{-m}\mathbf{S}_{\text{fb}}\mathbf{r}(j)| = 0$, i.e., $|\mathbf{e}_{ss}| = 0$. Therefore, if the condition (31) is satisfied, the steady-state error will converge to zero. It should be noted that although the reference trajectory $\mathbf{r}(j)$ still varies with time, the convergence of tracking error will also be guaranteed according to the abovementioned analysis through implementing the proposed method.

IV. EXPERIMENTAL SETUP

A. System Identification

The nanopositioning stage (P-561.3CD, Physik Instrumente), a piezoelectric stack-actuated platform based on parallel-kinematic design is used to evaluate the proposed controller. The experimental setup is showed in Fig. 5. The control input voltage (0–10 V) is produced by 16-b digital to analog converters of the data acquisition card (PCI 6289, National Instrument) and subsequently amplified via a piezo amplifier module (E-503.00, Physik Instrumente) to provide excitation voltage (0–100 V) for the nanopositioner. The output (0–10 V), which is normalized with respect to 0–100 μm , is read via a capacitive sensor monitor (E-509.C3A, Physik Instrumente) and is passed to the data acquisition card (PCI 6289, National Instrument). The overall

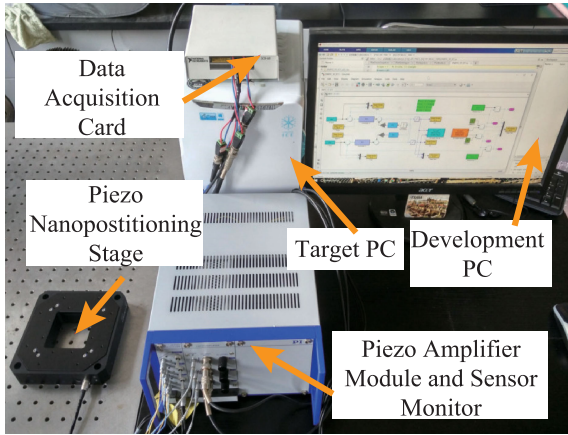


Fig. 5. Experimental setup of the piezoelectric nanopositioning stage.

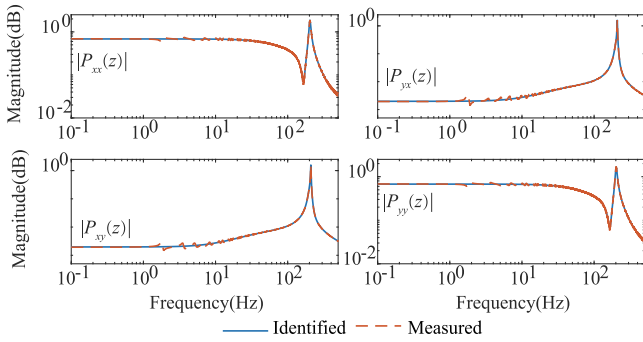


Fig. 6. Identified and measured amplitude responses of the stage.

control system is built in Simulink real-time environment on the host computer and executed real-time on the target computer. In order to identify the linear dynamic model of the piezoelectric nanopositioning stage, a sine-sweep input with a constant low amplitude with the frequencies between 0.1 and 500 Hz is applied to the x - and y -axis. After being discretized via zero-order holder method, the linear discrete transfer functions of x to x and y to x are given as

$$P_{xx}(z) = \frac{0.014z^4 - 0.054z^3 + 0.123^2 - 0.128z + 0.056}{z^5 - 3.82z^4 + 6.316z^3 - 5.54z^2 + 2.58z - 0.51} \quad (38)$$

$$P_{xy}(z) = \frac{0.002z^4 - 0.009z^3 + 0.016z^2 - 0.013z + 0.004}{z^5 - 4.016z^4 + 7.141z^3 - 6.87z^2 + 3.57z - 0.81} \quad (39)$$

The first resonant frequency of both x - and y -axis is 210 Hz from Fig. 6, which limits the motion within a low speed when implementing the stand-alone FBC. In addition, there exists cross-coupling effects according to Fig. 6 and it is especially obvious near the first resonant frequency. In this article, the cross-coupling error is considered as the external disturbance to simplify the implementation of the proposed controller. Note that although the nanopositioning stage cannot achieve video-rate imaging, the proposed controller can also be implemented on a stage with a higher resonant frequency.

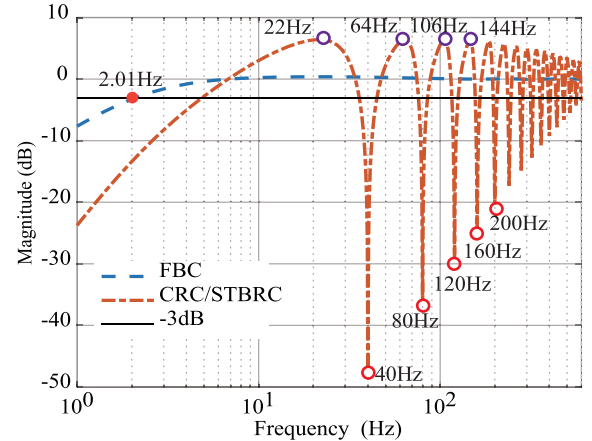


Fig. 7. Sensitivity transfer functions of the baseline FBC and CRC/STBRC for x -axis with a 40 Hz reference.

B. Controller Implementation

For the baseline FBC, a notch filter with an integral controller is designed primarily [36], where the notch filter's characteristic frequency is designed at 203 Hz to avoid the zero-pole cancellation as well as suppress the effect of the resonant peak, and a pair of poles are assigned at 2000 Hz to attenuate high-frequency noise. Furthermore, to improve the tracking performance, an integral gain 300 is cascaded before the notch filter. To facilitate the design of STBRC, the FBC is obtained by discretizing via bilinear transformation method as

$$C_x(z) = C_y(z) = \frac{0.0103z^3 - 0.0062z^2 - 0.0065z + 0.01}{z^3 - 2.111z^2 + 1.963z - 0.8519} \quad (40)$$

For the design of CRC and STBRC, the learning filters are calculated by the ZMET method using (15), and $a = 0.25$, $b = 0.5$ are chosen for the zero-phase low filter $Q(z)$. Because the nanopositioning stage is a nonminimum-phase system, the delay term m is determined as 3 for both x - and y -axis for the symmetric structure of the stage. The sensitivity transfer functions of x -axis for FBC, CRC, and STBRC are plotted in Fig. 7. In this article, the FBC in the proposed controller is designed with a sufficiently low bandwidth at 2.01 Hz to evaluate its advantage to tracking the high-speed trajectory and suppressing low-frequency disturbance, such as cross coupling and attenuate noises. Taking a 40 Hz reference as an example, STBRC can provide multiple lower gains at the fundamental frequency and its harmonics to ensure zero steady-state errors. It should be noted that when implementing CRC, $\Phi_{ST}(k)$ and $\Phi_{IST}(k)$, given as (11) and (12), are set as 1 and for STBRC.

In this article, a zero-phase low-pass filter is adopted to ensure the robustness of STBRC. Hence, \mathbf{Q} in (31) is a symmetric matrix instead of a lower triangular one. In spite of that, the stability condition is still correct for $\rho(\mathbf{E}) \approx \rho[\mathbf{Q}(\mathbf{I} - \mathbf{L}\mathbf{T}_{fb})]$, which can be concluded in Tables I and II, and the maximum eigenvalues without transformation terms are 0.891 and 0.887, respectively. Therefore, (32) can also be employed to ensure the stability and error convergence of STBRC with a zero-phase filter for spiral trajectory. Besides, the maximum eigenvalues in

TABLE I
MAXIMUM EIGENVALUE $\rho(\mathbf{E})$ AT DIFFERENT PERIODS FOR 40 Hz SPIRAL TRAJECTORY OF x -AXIS

j	2	5	15	20	25
$\rho(\mathbf{E})$	0.888	0.889	0.890	0.890	0.891

TABLE II
MAXIMUM EIGENVALUE $\rho(\mathbf{E})$ AT DIFFERENT PERIODS FOR 50 Hz SPIRAL TRAJECTORY OF y -AXIS

j	2	5	15	20	25
$\rho(\mathbf{E})$	0.885	0.886	0.887	0.887	0.887

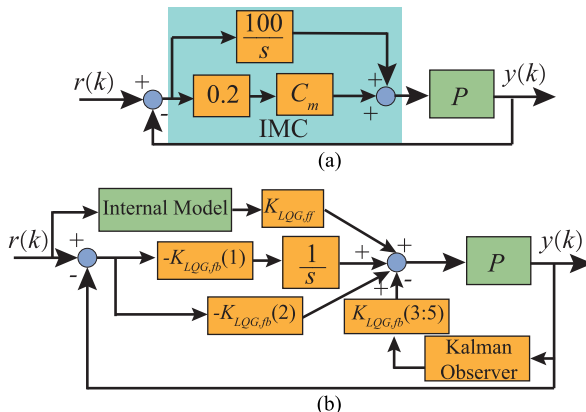


Fig. 8. Block diagram of other controllers in this article. (a) IMC. (b) IMLQG.

different periods are nearly the same, which demonstrates that the time-variant transformation terms have no influence on the stability.

V. COMPARATIVE EXPERIMENTS

A. Comparison With Internal Model Based Controllers

The IMC is also an effective method to track a known signal. In this section, an IMC in [19] and [20] based on H_∞ mixed-sensitivity synthesis [37] is designed to compare with the proposed STBRC. A stable sensitivity weight $W_S(s) = [1 + \frac{2 \times 10^{-4} s}{2\pi f} + (\frac{s}{2\pi f})^2]^{-2}$ and constant control weight $W_U(s) = 5$ are used in MATLAB function mixsyn. After reducing the order, the resulting IMC for 40 Hz spiral trajectory may be written as

$$C_m(s) = \frac{0.27 s^4 - 82 s^3 + 25370 s^2 - 7.9 \times 10^6 s - 2.5 \times 10^9}{s^4 + 0.1 s^3 + 1.26 \times 10^5 s^2 + 6350 s + 3.99 \times 10^9}. \quad (41)$$

An integral controller is also added to improve the steady-state precision, and the block diagram of this controller is implemented as given in Fig. 8(a). The final IMC controller is determined as

$$C_{\text{IMC}}(s) = \frac{100}{s} + 0.2C_m(s). \quad (42)$$

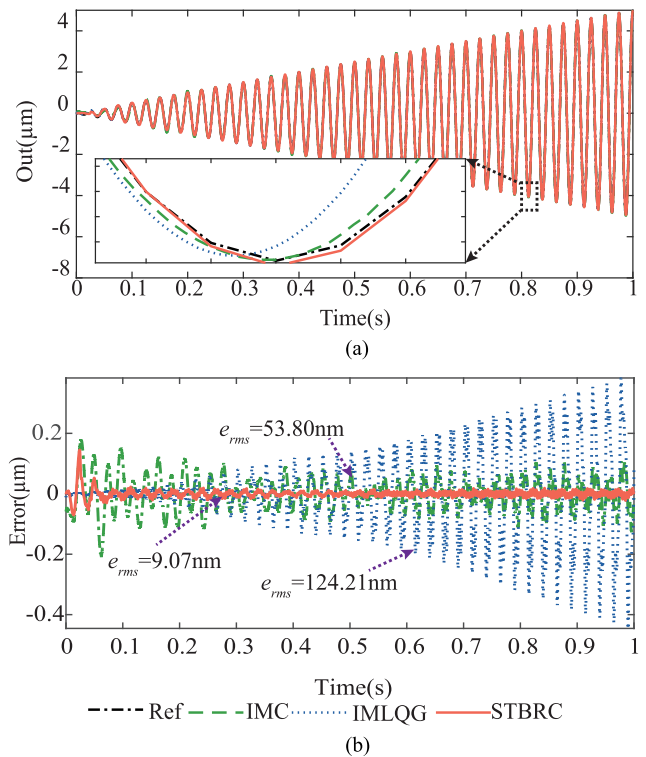


Fig. 9. Experimental results of IMC, IMLQG, and proposed STBRC of x -axis at 40 Hz spiral. (a) Spiral trajectory tracking. (b) Tracking errors.

Besides, an internal-model-based LQG controller (IMLQG) proposed in [18] is also designed as a benchmark in this article with block diagram in Fig. 8(b). In this method, the internal model of the reference sinusoidal signal is combined into the plant model, and an integrator is introduced with an LQG controller to improve the tracking performance. Additional, a Kalman observer with the variance of 0.002 and covariance matrix $10^{-6} \mathbf{I}_{5 \times 5}$ is employed to calculate the observer vector, and subsequently estimate the states of the plant in order to implement the state feedback control [20]. In this article, the weighting matrices are selected as $Q_{\text{LQG}} = \text{diag}[10^7 \ 0.008 \ 1 \ 1 \ 1]^\top$ and $R_{\text{LQG}} = 0.01$, respectively. Then, the feedback and feedforward gains are calculated as

$$\begin{aligned} K_{\text{LQG},\text{fb}} &= [-3162.2 \ -38.8 \ 2.7 \ 143.6 \ 304.3 \ 268.2] \\ K_{\text{LQG},\text{ff}} &= [-17.7 \ 3393.5]. \end{aligned} \quad (43)$$

The tracking results of 40 Hz spiral trajectory for internal model based controllers with a maximum 10 μm peak-to-peak amplitude are demonstrated in Fig. 9. Both the IMC and STBRC can achieve convergence of the steady-state errors as the increase of spiral amplitude, while the error of IMLQG increases with the amplitude with the root-mean-square errors (e_{rms}) 124.21 nm. This is because the model of the varying amplitude is not taken consideration into IMLQG [20]. In this article, only the fundamental frequency internal model at 40 Hz is built in (42) so that the e_{rms} is 53.80 nm in contrast to 9.07 nm with STBRC. The results show that the STBRC achieves the better performance than the IMC. The better performance can also

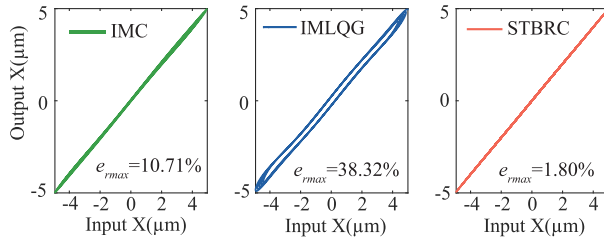


Fig. 10. Experimental results of the relations between actual displacements and the desired reference of x -axis at 40 Hz spiral.

be obtained by IMC with more high-frequency internal models contained in (42) at the cost of more parameters to be tuned, especially for different tracking frequencies. In comparison, the only parameter N is needed to be adjusted along with tracking frequency in the premise of stability condition (31).

To investigate the effect of hysteresis nonlinearity on the controllers, the results of the relations between the actual displacements and the desired reference are plotted in Fig. 10. The relative maximal errors (e_{rmax}) of the hysteresis loops for different controllers are 10.71%, 38.32%, and 1.80%, respectively, which demonstrates the proposed STBRC can mitigate hysteresis phenomenon effectively compared with other internal model based controllers.

B. Spiral Trajectory Tracking

1) *Suppression of Cross-Coupling Effect:* In this article, the controllers are designed separately for x - and y -axis by taking cross-coupling effects as disturbances. To validate the effectiveness of STBRC on suppression of cross-coupling errors, a 50 Hz spiral trajectory with a maximum 10 μm peak-to-peak amplitude is injected into the x -axis of the stage. It is clear that the cross-coupling errors increase with the amplitude and is drifting with time for open-loop (OL) result in Fig. 11. e_{rms} is 3.79 nm and 10.92 nm for standalone FBC and IMLQG, while CRC and STBRC achieve lower e_{rms} with 2.46 and 2.41 nm, respectively. The results show that the proposed controller can compensate for cross-coupling effects substantially.

2) *High-Speed Tracking Results:* The tracking performance of the proposed controller is tested with a spiral trajectory with a maximum 10 μm peak-to-peak amplitude at 40 and 50 Hz, respectively. The tracking results of XY spiral are demonstrated in Figs. 12 and 13. It can be concluded that both the OL and FBC have less scanning areas than the references (Ref) for the lower gains and higher delay at closed-loop high-frequency regions. The tracking errors of 40 Hz, 50 Hz for x - and y -axes are given in Figs. 14 and 15. It is evident that STBRC can make the steady-state error convergent after several circles through learning the last circle's error while the error of CRC remains the same with the increase of reference amplitude. This is because the error in the previous period is not repetitive in the current period, resulting in less control force of CRC. The error of IMLQG increases with time although its performance is better than OL and FBC.

The e_{rms} and maximal errors (e_{max}) are tabulated in Tables III and IV in detail. It should be noted that the error of FBC is larger

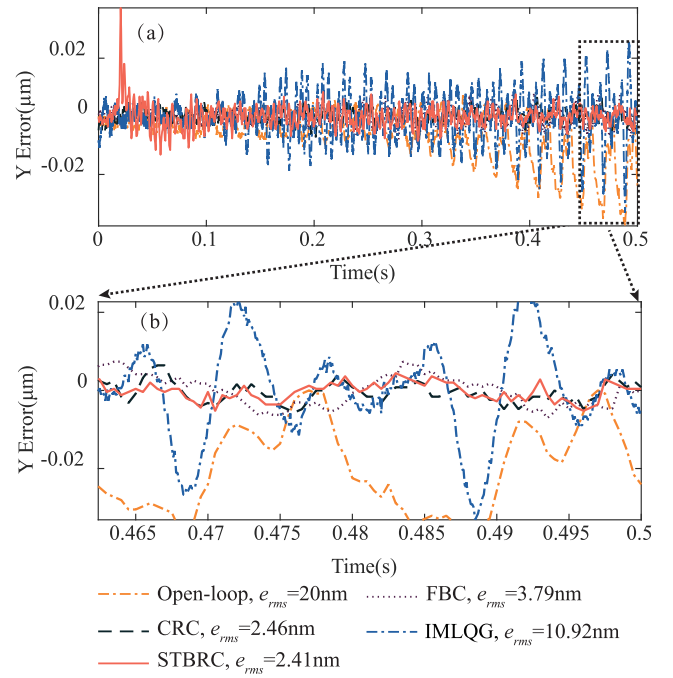


Fig. 11. Experimental results of cross-coupling effect for y -axis at 50 Hz spiral. (a) Cross-coupling errors of y -axis. (b) Zoomed-in view of the tracking errors.

TABLE III
STATISTICAL RESULTS OF STEADY-STATE TRACKING ERRORS WITH
40 Hz SPIRAL TRAJECTORY (UNIT:NM)

Statistical Errors(nm)	OL	FBC	CRC	IMLQG	STBRC
x axis	e_{rms}	2602.1	4137.2	118.43	249.89
	e_{max}	4071.5	6311.2	170.53	410.39
y axis	e_{rms}	2658.6	4173.2	112.49	240.42
	e_{max}	3946.3	6247.1	158.40	370.44

TABLE IV
STATISTICAL RESULTS OF STEADY-STATE TRACKING ERRORS WITH
50 Hz SPIRAL TRAJECTORY (UNIT:NM)

Statistical Errors(nm)	OL	FBC	CRC	IMLQG	STBRC
x axis	e_{rms}	2946.5	3923.1	148.72	318.95
	e_{max}	4702.7	6140.7	209.53	486.22
y axis	e_{rms}	3000.6	3918.9	139.89	346.44
	e_{max}	4510.8	5978.3	198.90	484.90

than that of OL due to the sensitivity bandwidth of the designed FB controller of 2.01 Hz in order to suppress disturbances and reduce projection noises. For the tracking performance of STBRC, e_{rms} and e_{max} of x at 50 Hz are 6.46 and 15.84 nm, respectively, in comparison with 148.72 and 209.53 nm of CRC, 318.95 and 486.22 nm of IMLQG. Also note that when the tracking frequency varies from 40 to 50 Hz, the statistical errors of STBRC are all within 6.5 and 18 nm, i.e., 0.065% and 0.18% of the maximum amplitude, respectively. A similar conclusion can also be drawn from the tracking performance of y -axis, which validates the effectiveness of STBRC. Besides, the hysteresis loops of different controllers at 50 Hz spiral with steady state

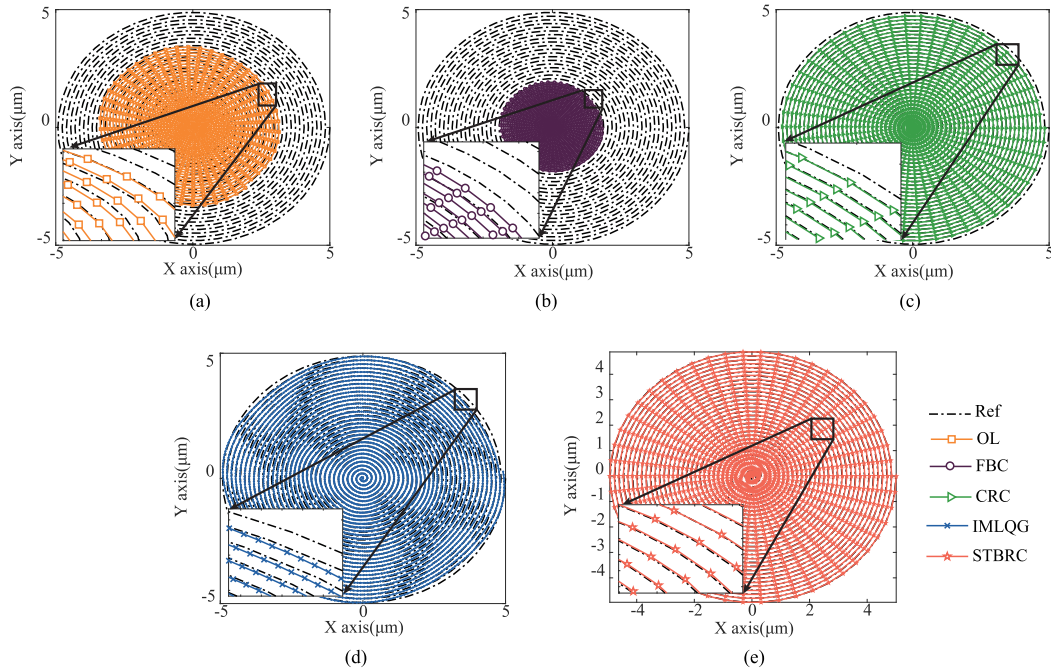


Fig. 12. Tracking results of different controllers for 40 Hz spiral trajectory. (a) OL. (b) FBC. (c) CRC. (d) IMLQG. (e) STBRC.

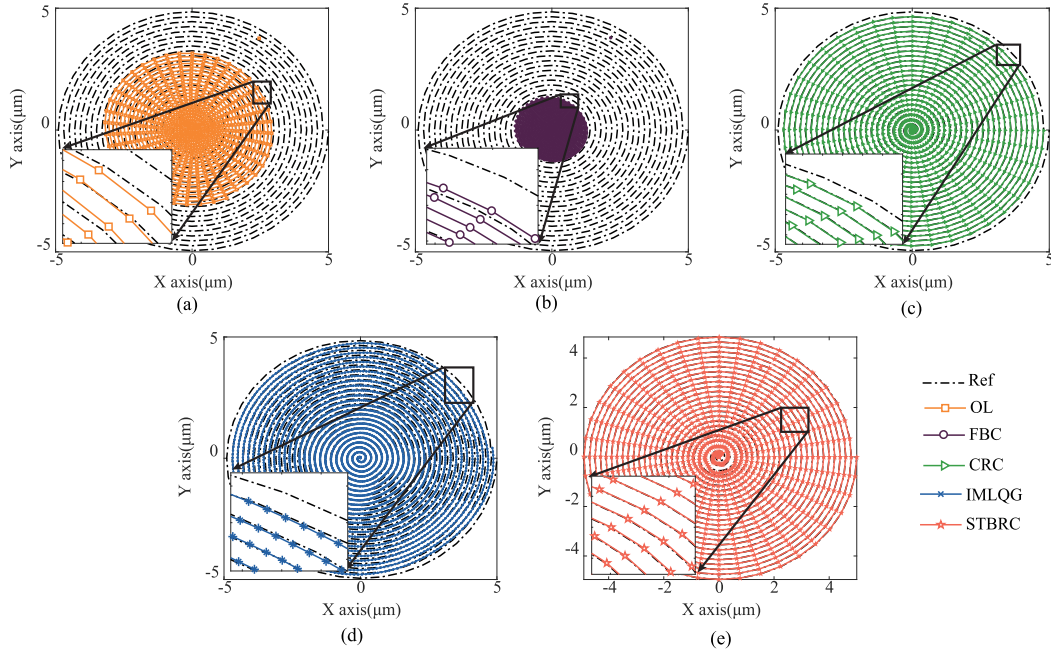


Fig. 13. Tracking results of different controllers for 50 Hz spiral trajectory. (a) OL. (b) FBC. (c) CRC. (d) IMLQG. (e) STBRC.

are also given in Fig. 16, where the $e_{r\max}$ of STBRC achieves 1.60%, showing the best performance among these controllers.

Note that in this section, two scenarios with 40 and 50 Hz spiral trajectories are tested to show the flexibility and adaptability of the proposed method at different frequencies primarily. The further improvement of the tracking speed on the nanopositioning stage in Fig. 5 is limited by the mechanical design and driving principle, and the system in this article is employed to verify the

effectiveness of the proposed controller on spiral tracking. The disturbances or uncertainties within the unmatched frequency regions as shown in Fig. 7 also deteriorate the performance of a higher speed tracking. In spite of this, the tracking frequency of 50 Hz reaches 23.81% of the first resonant frequency at 210 Hz, which achieves the best performance among the values of 21.57% in [15], 17.57% in [18] with piezoelectric actuator under fair comparisons.

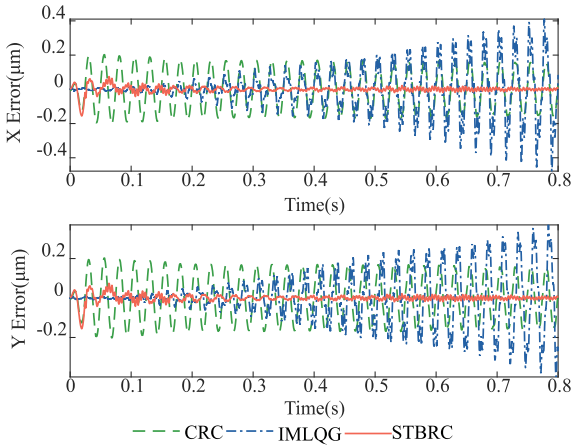


Fig. 14. Tracking errors of 40 Hz trajectory for x - and y -axis.

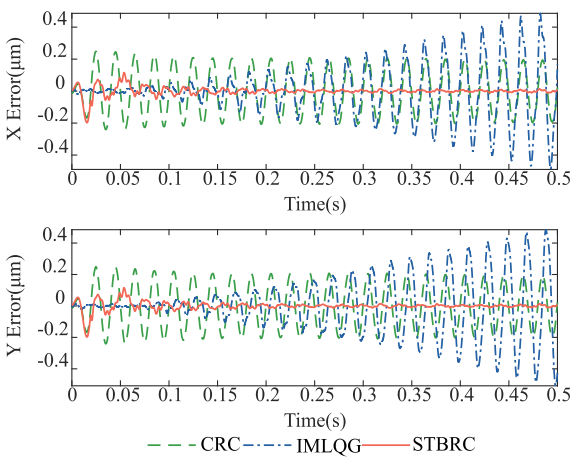


Fig. 15. Tracking errors of 50 Hz trajectory for x - and y -axis.

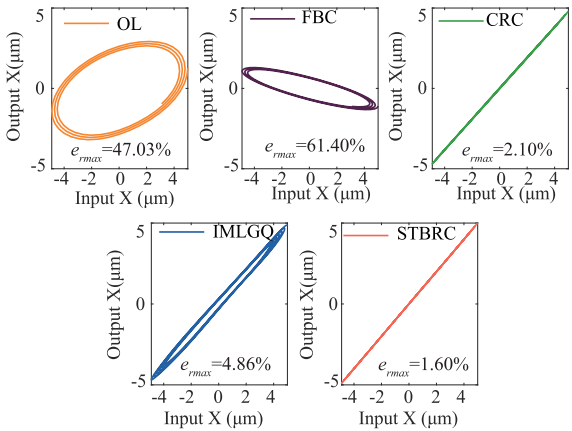


Fig. 16. Experimental results of the relations between actual displacements and the desired reference of x -axis at 50 Hz spiral with steady state.

VI. CONCLUSION

In this article, the STBRC was proposed for high-speed and high-precision tracking of spiral trajectory. Different from the signal transformation approach to map between piecewise reference signal and ramp signal, a transformation for spiral

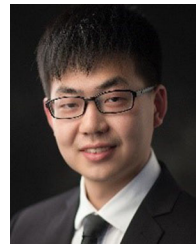
trajectory to constant amplitude sinusoid was designed. Through integrating with CRC, the STBRC can provide infinite internal models of spiral trajectory, even at high-frequency harmonics, to achieve convergent steady-state errors. The proposed method extends the application of CRC that requires strictly periodic signals. Due to the time-variant property of the overall system, the stability and error convergence of the STBRC is proven in a lifted-system representation. The experiments on a piezoelectric nanopositioning stage were also performed. Comparative results demonstrated that the proposed controller achieves the better performance than internal model based controllers with a simpler structure and fewer parameters. Furthermore, the cross-coupling e_{rms} was suppressed to 2.41 nm, and e_{rms} and e_{max} of both x - axis and y -axis are below 0.065% and 0.18% of the maximum amplitude for high-speed spiral tracking, showing the best performance through comparisons.

Despite that the proposed method can handle low-frequency disturbances effectively, the controller may amplify the disturbances that do not match with the fundamental frequency and its harmonics of reference, as is shown in Fig. 7. The future work will concentrate on dealing with this by employing disturbance observer technology.

REFERENCES

- [1] M. Ling, J. Cao, Z. Jiang, M. Zeng, and Q. Li, "Optimal design of a piezo-actuated 2-dof millimeter-range monolithic flexure mechanism with a pseudo-static model," *Mech. Syst. Signal Process.*, vol. 115, pp. 120–131, 2019.
- [2] S. M. Salapaka and M. V. Salapaka, "Scanning probe microscopy," *IEEE Control Syst. Mag.*, vol. 28, no. 2, pp. 65–83, Apr. 2008.
- [3] S. R. Moheimani, "Invited review article: Accurate and fast nanopositioning with piezoelectric tube scanners: Emerging trends and future challenges," *Rev. Sci. Instrum.*, vol. 79, no. 7, 2008, Art. no. 071101.
- [4] M. Rana, H. R. Pota, and I. R. Petersen, "Improvement in the imaging performance of atomic force microscopy: A survey," *IEEE Trans. Autom. Sci. Eng.*, vol. 14, no. 2, pp. 1265–1285, Apr. 2017.
- [5] G.-Y. Gu, L.-M. Zhu, C.-Y. Su, H. Ding, and S. Fatikow, "Modeling and control of piezo-actuated nanopositioning stages: A survey," *IEEE Trans. Autom. Sci. Eng.*, vol. 13, no. 1, pp. 313–332, Jan. 2016.
- [6] J. Y. Lau, W. Liang, and K. K. Tan, "Adaptive sliding mode enhanced disturbance observer-based control of surgical device," *ISA Trans.*, vol. 90, pp. 178–188, 2019.
- [7] J. P. Mishra, Q. Xu, X. Yu, and M. Jalili, "Precision position tracking for piezoelectric-driven motion system using continuous third-order sliding mode control," *IEEE/ASME Trans. Mechatronics*, vol. 23, no. 4, pp. 1521–1531, Aug. 2018.
- [8] Q. Xu, "Precision motion control of piezoelectric nanopositioning stage with chattering-free adaptive sliding mode control," *IEEE Trans. Autom. Sci. Eng.*, vol. 14, no. 1, pp. 238–248, Jan. 2017.
- [9] H. Habibullah, H. Pota, I. R. Petersen, and M. Rana, "Tracking of triangular reference signals using LQG controllers for lateral positioning of an AFM scanner stage," *IEEE/ASME Trans. Mechatronics*, vol. 19, no. 4, pp. 1105–1114, Aug. 2014.
- [10] M. Namavar, A. J. Fleming, M. Aleyaasin, K. Nakkeeran, and S. S. Aphale, "An analytical approach to integral resonant control of second-order systems," *IEEE/ASME Trans. Mechatronics*, vol. 19, no. 2, pp. 651–659, Apr. 2014.
- [11] J. Ling, M. Rakotondrabe, Z. Feng, M. Ming, and X. Xiao, "A robust resonant controller for high-speed scanning of nanopositioners: Design and implementation," *IEEE Trans. Control Syst. Technol.*, to be published, doi: 10.1109/TCST.2019.2899566.
- [12] Y. R. Teo, Y. Yong, and A. J. Fleming, "A comparison of scanning methods and the vertical control implications for scanning probe microscopy," *Asian J. Control*, vol. 20, no. 4, pp. 1352–1366, 2018.
- [13] I. A. Mahmood, S. R. Moheimani, and B. Bhikkaji, "A new scanning method for fast atomic force microscopy," *IEEE Trans. Nanotechnol.*, vol. 10, no. 2, pp. 203–216, Mar. 2011.

- [14] M. Rana, H. Pota, and I. Petersen, "Spiral scanning with improved control for faster imaging of AFM," *IEEE Trans. Nanotechnol.*, vol. 13, no. 3, pp. 541–550, May 2014.
- [15] H. Pota *et al.*, "Reduction of phase error between sinusoidal motions and vibration of a tube scanner during spiral scanning using an AFM," *Int. J. Control. Autom.*, vol. 14, no. 2, pp. 505–513, 2016.
- [16] B. A. Francis and W. M. Wonham, "The internal model principle of control theory," *Automatica*, vol. 12, no. 5, pp. 457–465, 1976.
- [17] A. Bazaei, Y. K. Yong, and S. R. Moheimani, "High-speed lissajous-scan atomic force microscopy: Scan pattern planning and control design issues," *Rev. Sci. Instrum.*, vol. 83, no. 6, 2012, Art. no. 063701.
- [18] H. Habibullah, H. R. Pota, and I. R. Petersen, "A novel control approach for high-precision positioning of a piezoelectric tube scanner," *IEEE Trans. Autom. Sci. Eng.*, vol. 14, no. 1, pp. 325–336, Jan. 2017.
- [19] A. Bazaei, M. Maroufi, A. G. Fowler, and S. R. Moheimani, "Internal model control for spiral trajectory tracking with MEMS AFM scanners," *IEEE Trans. Control Syst. Technol.*, vol. 24, no. 5, pp. 1717–1728, Sep. 2016.
- [20] A. Bazaei, Y. K. Yong, and S. R. Moheimani, "Combining spiral scanning and internal model control for sequential AFM imaging at video rate," *IEEE/ASME Trans. Mechatronics*, vol. 22, no. 1, pp. 371–380, Feb. 2017.
- [21] C.-X. Li, G.-Y. Gu, L.-M. Zhu, and C.-Y. Su, "Odd-harmonic repetitive control for high-speed raster scanning of piezo-actuated nanopositioning stages with hysteresis nonlinearity," *Sensors Actuat. A-Phys.*, vol. 244, pp. 95–105, 2016.
- [22] T. Tang, S. X. Niu, T. Yang, B. Qi, and Q. L. Bao, "Vibration rejection of tip-tilt mirror using improved repetitive control," *Mech. Syst. Signal Process.*, vol. 116, pp. 432–442, 2019.
- [23] Z. Zhang, X. Yang, and P. Yan, "Large dynamic range tracking of an xy compliant nanomanipulator with cross-axis coupling reduction," *Mech. Syst. Signal Process.*, vol. 117, pp. 757–770, 2019.
- [24] H. Tang *et al.*, "Development and repetitive-compensated PID control of a nanopositioning stage with large-stroke and decoupling property," *IEEE Trans. Ind. Electron.*, vol. 65, no. 5, pp. 3995–4005, May 2018.
- [25] Z. Feng, J. Ling, M. Ming, and X. Xiao, "Integrated modified repetitive control with disturbance observer of piezoelectric nanopositioning stages for high-speed and precision motion," *J. Dyn. Syst., Meas. Control*, vol. 141, no. 8, 2019, Art. no. 081006.
- [26] A. Bazaei, S. R. Moheimani, and A. Sebastian, "An analysis of signal transformation approach to triangular waveform tracking," *Automatica*, vol. 47, no. 4, pp. 838–847, 2011.
- [27] T. Tuma, A. Pantazi, J. Lygeros, and A. Sebastian, "Comparison of two non-linear control approaches to fast nanopositioning: Impulsive control and signal transformation," *Mechatronics*, vol. 22, no. 3, pp. 302–309, 2012.
- [28] A. Bazaei, S. R. Moheimani, and Y. K. Yong, "Improvement of transient response in signal transformation approach by proper compensator initialization," *IEEE Trans. Control Syst. Technol.*, vol. 22, no. 2, pp. 729–736, Mar. 2014.
- [29] A. Bazaei, Z. Chen, Y. K. Yong, and S. R. Moheimani, "A novel state transformation approach to tracking of piecewise linear trajectories," *IEEE Trans. Control Syst. Technol.*, vol. 26, no. 1, pp. 128–138, Jan. 2018.
- [30] A. Bazaei and S. O. R. Moheimani, "Signal transformation approach to tracking control with arbitrary references," *IEEE Trans. Autom. Control*, vol. 57, no. 9, pp. 2294–2307, Sep. 2012.
- [31] J. C. Doyle, B. A. Francis, and A. R. Tannenbaum, *Feedback Control Theory*. Chelmsford, MA, USA: Courier Corporation, 2013.
- [32] C. Lee and S. M. Salapaka, "Robust broadband nanopositioning: Fundamental trade-offs, analysis, and design in a two-degree-of-freedom control framework," *Nanotechnology*, vol. 20, no. 3, 2008, Art. no. 035501.
- [33] J. Butterworth, L. Pao, and D. Abramovitch, "Analysis and comparison of three discrete-time feedforward model-inverse control techniques for nonminimum-phase systems," *Mechatronics*, vol. 22, no. 5, pp. 577–587, 2012.
- [34] J. Li and T.-C. Tsao, "Robust performance repetitive control systems," *J. Dyn. Sys., Meas., Control*, vol. 123, no. 3, pp. 330–337, 1998.
- [35] D. A. Bristow, M. Tharayil, and A. G. Alleyne, "A survey of iterative learning control," *IEEE Control Syst. Mag.*, vol. 26, no. 3, pp. 96–114, Jun. 2006.
- [36] K. K. Leang and S. Devasia, "Feedback-linearized inverse feedforward for creep, hysteresis, and vibration compensation in AFM piezoactuators," *IEEE Trans. Control Syst. Technol.*, vol. 15, no. 5, pp. 927–935, Sep. 2007.
- [37] S. Skogestad and I. Postlethwaite, *Multivariable Feedback Control: Analysis and Design*, vol. 2. New York, NY, USA: Wiley, 2007.



Zhao Feng (Student Member, IEEE) received the B.S. degree in mechanical engineering in 2010 from the School of Power and Mechanical Engineering, Wuhan University, Wuhan, China, where he is currently working toward the Ph.D. degree in mechanical engineering.

He is currently a Visiting Ph.D. Student with the Department of Electrical and Computer Engineering, National University of Singapore, Singapore. His research interests include vibration control, iterative learning control, nanopositioning,

ing and robotics.



Jie Ling (Member, IEEE) received the B.S. and Ph.D. degrees in mechanical engineering from the School of Power and Mechanical Engineering, Wuhan University, Wuhan, China, in 2012 and 2018, respectively.

He was a Joint Ph.D. Student with the Department of Automatic Control and Micro-Mechatronic Systems, FEMTO-st Institute, Besançon, France, in 2017. Since 2019, he has been a Joint Postdoctoral Researcher with the Department of Biomedical Engineering, National University of Singapore, Singapore. Since 2018, he has been a Postdoctoral Researcher with the Department of Mechanical Engineering, Wuhan University. His research interests include mechanical design and precision motion control of nanopositioning stages and micromanipulation robots.



Min Ming received the B.S. degree in mechanical engineering in 2014 from the School of Power and Mechanical Engineering, Wuhan University, Wuhan, China, where he is currently working toward the Ph.D. degree in mechanical engineering.

Her research interest covers hysteresis compensation, iterative learning control, and nano-positioner.



Wenyu Liang (Member, IEEE) received the B.Eng. and M.Eng. degrees in mechanical engineering from the China Agricultural University, Beijing, China, in 2008 and 2010, respectively, and the Ph.D. degree in electrical and computer engineering from the National University of Singapore, Singapore, in 2014.

He is currently an Adjunct Assistant Professor with the Department of Electrical and Computer Engineering, National University of Singapore. His research interests mainly include robotics, mechatronics and automatic, precision motion control, and force control with applications in medical and industrial technology.



Kok Kiong Tan (Member, IEEE) received the B.Eng. and Ph.D. degrees in electrical and computer engineering from the Department of Electrical and Computer Engineering, National University of Singapore, Singapore, in 1992 and 1995, respectively.

Prior to joining the National University of Singapore, he was a Research Fellow with the Singapore Institute of Manufacturing Technology, Singapore, a National R&D Institute spearheading the promotion of R&D in local manufacturing industries, where he was involved in managing industrial projects. He was a Professor with the National University of Singapore. He has authored or coauthored more than 200 journal papers to date and has written 14 books, all resulting from research in these areas. His current research interests include precision motion control and instrumentation, advanced process control and auto-tuning, and general industrial automation.



Xiaohui Xiao (Member, IEEE) received the B.S. and M.S. degrees from Wuhan University, Wuhan, China, in 1991 and 1998, respectively, and the Ph.D. degree from the Huazhong University of Science and Technology, Wuhan, in 2005, all in mechanical engineering.

In 1998, she joined the Wuhan University, Wuhan, where she is currently a Full Professor with the Mechanical Engineering Department, School of Power and Mechanical Engineering. Her current research interests include mobile robotics, high-precision positioning control, and signal processing.